



# Machine learning atomic dynamics to unfold the origin of plasticity in metallic glasses: From thermo- to acousto-plastic flow

Xiaodi Liu<sup>1,2</sup>, Quanfeng He<sup>3</sup>, Wenfei Lu<sup>4</sup>, Ziqing Zhou<sup>3</sup>, Jinsen Tian<sup>1</sup>, Dandan Liang<sup>5</sup>, Jiang Ma<sup>1</sup>, Yong Yang<sup>3,6</sup> and Jun Shen<sup>1,2\*</sup>

**ABSTRACT** Metallic glasses (MGs) have an amorphous atomic arrangement, but their structure and dynamics in the nanoscale are not homogeneous. Numerous studies have confirmed that the static and dynamic heterogeneities of MGs are vital for their deformation mechanism. The “defects” in MGs are envisaged to be structurally loosely packed and dynamically active to external stimuli. To date, no definite structure-property relationship has been established to identify liquid-like “defects” in MGs. In this paper, we proposed a machine-learned “defects” from atomic trajectories rather than static structural signatures. We analyzed the atomic motion behavior at different temperatures *via* a *k*-nearest neighbors machine learning model, and quantified the dynamics of individual atoms as the machine-learned temperature. Applying this new temperature-like parameter to MGs under stress-induced flow, we can recognize which atoms respond like “liquids” to the applied loads. The evolution of liquid-like regions reveals the dynamic origin of plasticity (thermo- and acousto-plasticity) of MGs and the correlation between stress-induced heterogeneity and local environment around atoms, providing new insights into thermo- and acousto-plastic forming.

**Keywords:** metallic glass, plasticity, machine learning, molecular dynamics simulation

## INTRODUCTION

Since the first fabrication in 1960, metallic glasses (MGs) have blossomed into a revolutionary new class of functional materials with a combination of outstanding properties, such as high strength, large elastic limit, and soft magnetism, which place MGs among the most actively studied glasses and alloys [1–4]. The macroscopic properties of MGs are usually homogeneous and isotropic because MGs exhibit an amorphous structure without the long-range translational symmetry [5]. By contrast, MGs have structural and dynamic heterogeneity in the nanoscale and possess a short-range to medium-range order [5]. Extensive experimental and computational studies [1,3,6–8]

emphasized that nanoscale heterogeneity is crucial to unfold the mechanisms of deformation, crystallization, and relaxation behaviors of MGs.

Unlike the purely structural defects (e.g., dislocations) in crystals, several nanometer-sized local regions in MGs serve as “defects,” which are susceptible to external stimuli (such as temperature, applied quasi-static and cyclic dynamic loads) and often termed liquid-like regions [9] or flow units [10]. On these liquid-like sites, the activated atoms rearrange the configuration, taking responsibility for structural relaxation or plastic events in MGs. The isolated atomic rearrangement corresponds to  $\beta$  relaxation and the local shear transformation [9,11]. The percolation of liquid-like regions throughout the system signifies  $\alpha$  relaxation and overall stress-induced plastic flows [12–14]. The recent discovery of fast  $\beta'$  relaxation is associated with the localized atomic shuffling involving fewer atoms [15–17]. From the perspective of potential energy landscape, both the complex structural relaxation and the deformation mechanism of MGs can be depicted as stress-augmented thermal activation processes with different energy barriers [13,18–21]. According to the cooperative shear model [13,22], temperature and applied stresses play equivalent roles in altering energy barriers, differing only in the manner of scaling or biasing. Assuming the barrier hopping event to be a stochastic process instead of a deterministic process, the stochastic shear transformation model [23] can elucidate the creep (cold flow) mechanism of MGs from the activation and accumulation of liquid-like regions. In addition to cold flow, the recent studies reported that ultrasonic-vibration-induced plasticity (acousto-plastic flow) enables fast cold joining of MGs and fabrication of hybrid MGs [24,25]. The fast surface dynamics and cyclic-loading-induced liquefaction are possibly attributed to the enhanced atomic mobility at liquid-like sites, which is activated by external driving frequency approaching intrinsic relaxation frequency.

Over the past decades, considerable efforts have been exerted to identify liquid-like “defects” in MGs. The one who believed the existence of a priori structure of “defects” attempted to determine liquid-like regions only from the static structural signature. Such purely structural descriptors include free volume

<sup>1</sup> College of Mechatronics and Control Engineering, Shenzhen University, Shenzhen 518060, China

<sup>2</sup> Guangdong Key Laboratory of Electromagnetic Control and Intelligent Robots, Shenzhen University, Shenzhen 518060, China

<sup>3</sup> Department of Mechanical Engineering, College of Engineering, City University of Hong Kong, Kowloon Tong, Kowloon, Hong Kong SAR, China

<sup>4</sup> School of Materials Science and Engineering, Tongji University, Shanghai 201804, China

<sup>5</sup> Shanghai Engineering Research Center of Physical Vapor Deposition (PVD) Superhard Coating and Equipment, Shanghai Institute of Technology, Shanghai 201418, China

<sup>6</sup> Department of Materials Science and Engineering, College of Engineering, City University of Hong Kong, Kowloon Tong, Kowloon, Hong Kong SAR, China

\* Corresponding author (email: [junshen@szu.edu.cn](mailto:junshen@szu.edu.cn))

[26], bond orientational order (BOO) parameters [27,28], local structural entropy [29], tetrahedral-packed irregularity [30,31], Voronoi polyhedron [2,32], and various Voronoi-polyhedral derivatives, such as local fivefold symmetry [33], geometrical unfavored motif (GUM) [34], bond length deviation [35], and  $Q_k$  parameter [36]. These short-range order descriptors succeed in characterizing structural heterogeneity, but they cannot provide adequate information to account for property variation. In addition, the combination of local atomic packing with the thermodynamic or dynamic information formed an extended notion of structural indicators, such as soft mode [37,38], local thermal energy [39], vibrational mean squared displacement (vMSD) [40,41], and diverse vMSD-based parameters, such as directionally vMSD [42] and flexibility volume [43]. These indicators partly reveal the dynamic heterogeneity in MGs, but whether a one-to-one correspondence exists between the structure and property of liquid-like regions in MGs remains unclear and open for discussion.

The expression of liquid-like atomic sites literally implies the active atomic motion at high “temperatures”. A question naturally arises as to how “hot” liquid-like regions behave, which inspired us to design a temperature-like parameter for quantifying the mobility of atoms and further for recognizing liquid-like atoms (LAs) in response to external stimuli. To map a given temperature to mobility of individual atoms, we expected machine learning (ML) to be a promising technique. In view of the successful applications of ML to the evaluation of glass-forming ability [44–48], pioneering work has been conducted on machine-learned “defects,” such as softness [49], quench-in softness [50], structural flexibility [51], atomic-scale stiffness [52], integrated glassy defect [53], etc. [54–56]. However, these machine-learned indicators either only involve local structural signatures but neglect dynamic information, or fail to apply to high-stressed or high-temperature systems.

This paper aimed to identify liquid-like “defects” in MGs from the viewpoint of atomic dynamics. A temperature-like parameter  $T_{\text{ML}}$  was proposed from the  $k$ -nearest neighbors ( $k$ NN) ML model to evaluate the mobility of individual atoms. Applying  $T_{\text{ML}}$  to the MG samples undergoing thermo- and acousto-plastic deformation, we quantitatively understood the dynamic origin of plasticity of MGs from the evolution of high- $T_{\text{ML}}$  liquid-like regions, which also reveal the correlation with the structural and chemical characteristics.

## COMPUTATIONAL METHODS

### Classical MD simulation

The MD simulations were carried out using the large-scale atomic/molecular massively parallel simulator. The model  $\text{Cu}_{50}\text{Zr}_{50}$  system contained 50,000 atoms and had the dimension of  $\sim 10 \text{ nm} \times 10 \text{ nm} \times 10 \text{ nm}$ , and it was subjected to periodic boundary conditions for all three dimensions. The atomic interactions were described by the embedded atom method potential [57]. To obtain a glassy state, we initially melted the model at 2000 K, equilibrated it for 500 ps, and subsequently quenched it to different temperatures (from 100 to 1700 K) at a cooling rate of  $10^{11} \text{ K s}^{-1}$ . The whole process was in the isothermal-isobaric ensemble controlled at specified temperature and zero pressure by the Nosé-Hoover thermostat and barostat.

Determined by the volume-temperature curve in Supplementary information Fig. S1, the glass transition temperature  $T_g$

is 685 K, which is higher than the experimental measurement (670 K) [58], due to the cooling rate effect. The yield strengths were obtained from the tensile simulations, which were performed at a constant strain rate of  $0.0017 \text{ ps}^{-1}$  (corresponding to the loading rate of  $\sim 0.1 \text{ MPa fs}^{-1}$ ). To simulate creep, a series of uniaxial compressive stresses along the  $z$  direction were applied to the model MGs at the stress rate of  $0.1 \text{ MPa fs}^{-1}$  and held for 470 ps at  $T = 100, 200$ , and  $300 \text{ K}$ . The results of creep simulation can be found in Supplementary information. To mimic acousto-plastic flows, we exerted a sinusoidal stress on MG samples causing a tensile-compressive deformation at  $100 \text{ K}$ , with the stress amplitude  $\sigma_0 = 1.6 \text{ GPa}$  and driving frequency  $f = 2.0 \times 10^{10}, 5.0 \times 10^{10}$ , and  $1.0 \times 10^{11} \text{ s}^{-1}$ .

### Machine learning

A  $k$ NN model was established to correlate temperature and atomic mobility. Temperatures (from  $T = 100$  to  $1700 \text{ K}$ ) were initially applied to the class label candidates in this multiclass classifier, and the logarithms of square displacements scaled by temperatures  $\lg(\Delta r^2 / T)$  at different time intervals  $\Delta t$  (from  $0.01$  to  $200 \text{ ps}$ ) were chosen as the feature candidates of atomic mobility. The reason for the expression of atomic mobility was elucidated in the DISCUSSION section. To eliminate redundant temperature classes and improve the predictive accuracy, the temperature classes difficult to be distinguished should be ruled out. By using the agglomerative hierarchical clustering algorithm (see Supplementary information), seven representative classes, namely,  $T = 100, 700, 800, 900, 1000, 1200$ , and  $1700 \text{ K}$  were selected. To filter unnecessary features, the features in a short time ( $\Delta t \leq 0.1 \text{ ps}$ ) were removed on the basis of the ReliefF method (see Supplementary information). The dataset for training and testing consisted of the MD simulation results at different temperatures. Each atom corresponds to an instance. The atomic motion behavior was predicted by the  $k$ NN algorithm and 10-fold cross-validation method, in which the hyperparameters and data preprocessing were specified in Supplementary information. The ML was implemented by MATLAB R2020a.

## RESULTS

### $k$ NN model performance and machine-learned temperature

The training set consisted of the molecular dynamics (MD) simulation results of the  $\text{Cu}_{50}\text{Zr}_{50}$  MG samples at different temperatures. Each atom corresponds to an instance. In our  $k$ NN multiclass classifier, temperatures are the class labels, and atomic mobility characteristics are the ML features. To predict which class (i.e., temperature) an individual atom belongs to, the  $k$ NN model compared the features of the test atom with every instance in the training set and found out 50 nearest neighbors, representing 50 closest atoms in atomic dynamics. The machine-learned temperature  $T_{\text{ML}}$  of the atom is defined as the average of temperature labels of these nearest neighbors. Here, we must clarify that “the temperature of an atom” is a class label, denoting the applied temperature of the system which the atom probably belongs to.

Fig. 1 reveals a generally linear relation of the predicted temperatures to the actual values, proving that the  $k$ NN model is able to accurately describe the atomic motion in response to thermal agitation. The overestimation of  $T_{\text{actual}} = 100 \text{ K}$  resulted from misclassification of several instances to high- $T$  classes,

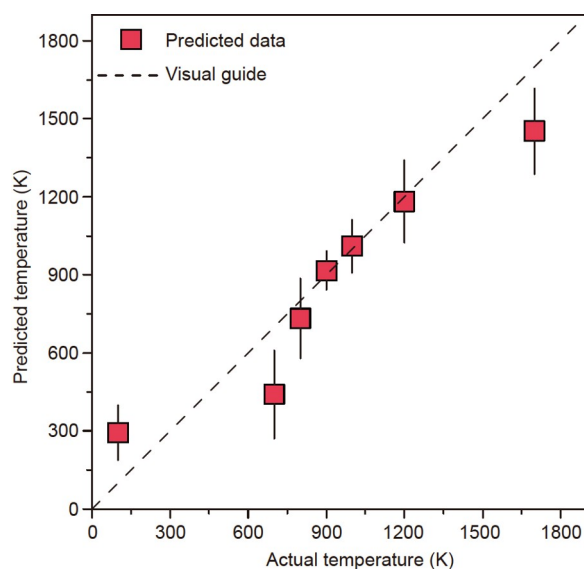


**Figure 1** Predicted vs. actual temperatures.

whereas the underestimation of  $T_{\text{actual}} = 700$  and  $1700$  K was caused by the opposite situation.

Different from the actual temperature,  $T_{\text{ML}}$  is a temperature-like descriptor about atomic dynamics, referring to the motion behavior of individual atoms under thermal stimulus. A high  $T_{\text{ML}}$ , e.g.,  $1000$  K, denotes that the atom is very mobile, and the atomic motion behaves like “a hot atom” at  $T = 1000$  K. Therefore, we can designate the atoms with  $T_{\text{ML}} > T_g$  or  $T_{\text{ML}} < T_g$  as the LAs or solid-like atoms (SAs). It is worth noting that LAs and SAs are defined from dynamic characteristics rather than structural signatures. Hence, LAs and SAs do not have to correspond to a specific static local structure, different from previous structural parameters.

### Machine-learned temperature of the MGs during creep

In view of the success of  $T_{\text{ML}}$  in characterizing the atomic dynamics under thermal stimulus, a creative application of  $T_{\text{ML}}$  is to make predictions for the atoms in an MG sample undergoing mechanical stimulus, such as creep (also called cold flow, which can be viewed as a thermoplastic flow). As the cases in point, the probability density distributions of  $T_{\text{ML}}$  with the applied stresses of  $\sigma_h = 2.2$  and  $2.3$  GPa at  $T = 100$  K are plotted

in Fig. 2a, b. And the results of other simulation conditions can be seen in Fig. S2. Firstly, there is an evident stress-induced heterogeneity in both conditions. At  $\sigma_h = 2.2$  GPa, the  $T_{\text{ML}}$  is distributed in a wide range with two maxima. One maximum is observed at  $\sim 270$  K, corresponding to the thermal contribution, which is consistent with the prediction in Fig. 1, and the other one is noted at  $\sim 790$  K, undoubtedly resulting from the quasi-statically mechanical input.  $T_{\text{ML}}$  quantitatively measures the extra atomic motion stemming from the mechanical agitations. At  $\sigma_h = 2.3$  GPa, the non-Gaussian distribution reveals the stress-induced dynamic heterogeneity, which suggests the existence of multiple characteristic  $T_{\text{ML}}$  in the sample. In contrast to the  $T_{\text{ML}}$  distributions of  $\sigma_h = 2.2$  GPa, the maximum at low  $T_{\text{ML}}$  vanishes but the high- $T_{\text{ML}}$  one develops. This finding indicates that the stress has dominated the overall behavior of atomic dynamics. It is interesting to observe more LAs with  $T_{\text{ML}} > T_g$  when the applied stress increases, which echoes the viewpoint that plastic deformation is a stress-induced glass transition [14,59]. Because thermal and mechanical agitations play similar roles in changing the energy state and amorphous structure of MGs [14,19,22], the MG samples will flow under incessantly high stress, though the temperature is far below  $T_g$  [14].

Secondly, the  $T_{\text{ML}}$  distribution evolves in different manners as the applied stress varies. Unlike the unstressed MGs, in which energy is conserved, the stressed MGs do not have the time translation symmetry. Therefore, the  $T_{\text{ML}}$  distribution, as well as MSD [17], will evolve as the start time changes. For  $\sigma_h = 2.2$  GPa, the high- $T_{\text{ML}}$  maximum slightly diminishes and then stabilizes, in line with the variation in strain rate (Fig. S3). This temporal evolution manner indicates the dominance of temperature. At a temperature far below  $T_g$ , such quasi-statically mechanical stimulus is too feeble to provide a sufficient cumulative probability for the irreversible transitions to reach the critical value within the time window, agreeing with the stochastic shear transformation model. However, for  $\sigma_h = 2.3$  GPa, the maximum near  $T_g$  continuously builds up during the primary and secondary creep stages, and this finding is associated with the increasing number of the SAs turning into the LAs. Subsequently, the distribution shifts toward the high  $T_{\text{ML}}$  over time, especially after the accumulative strain exceeds yield strain  $\varepsilon_y$ , i.e.,  $t > 100$  ps. This evolution behavior confirms that applying high stresses enhances the atomic mobility and promotes the irreversible barrier hopping events. Under high stresses, the number of local yielding events will reach the percolation limit and ultimately trigger the overall plastic flow.

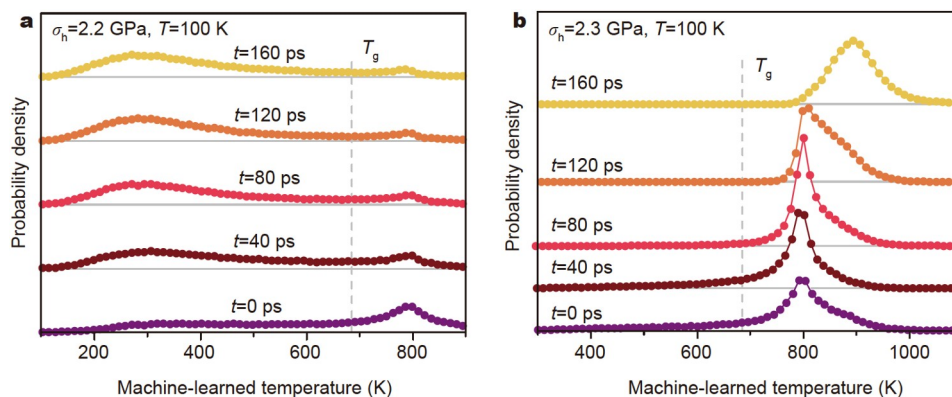


**Figure 2**  $T_{\text{ML}}$  distributions at  $100$  K with the applied stresses of (a)  $\sigma_h = 2.2$  GPa; and (b)  $2.3$  GPa.  $T_g$  is represented by the dashed line.



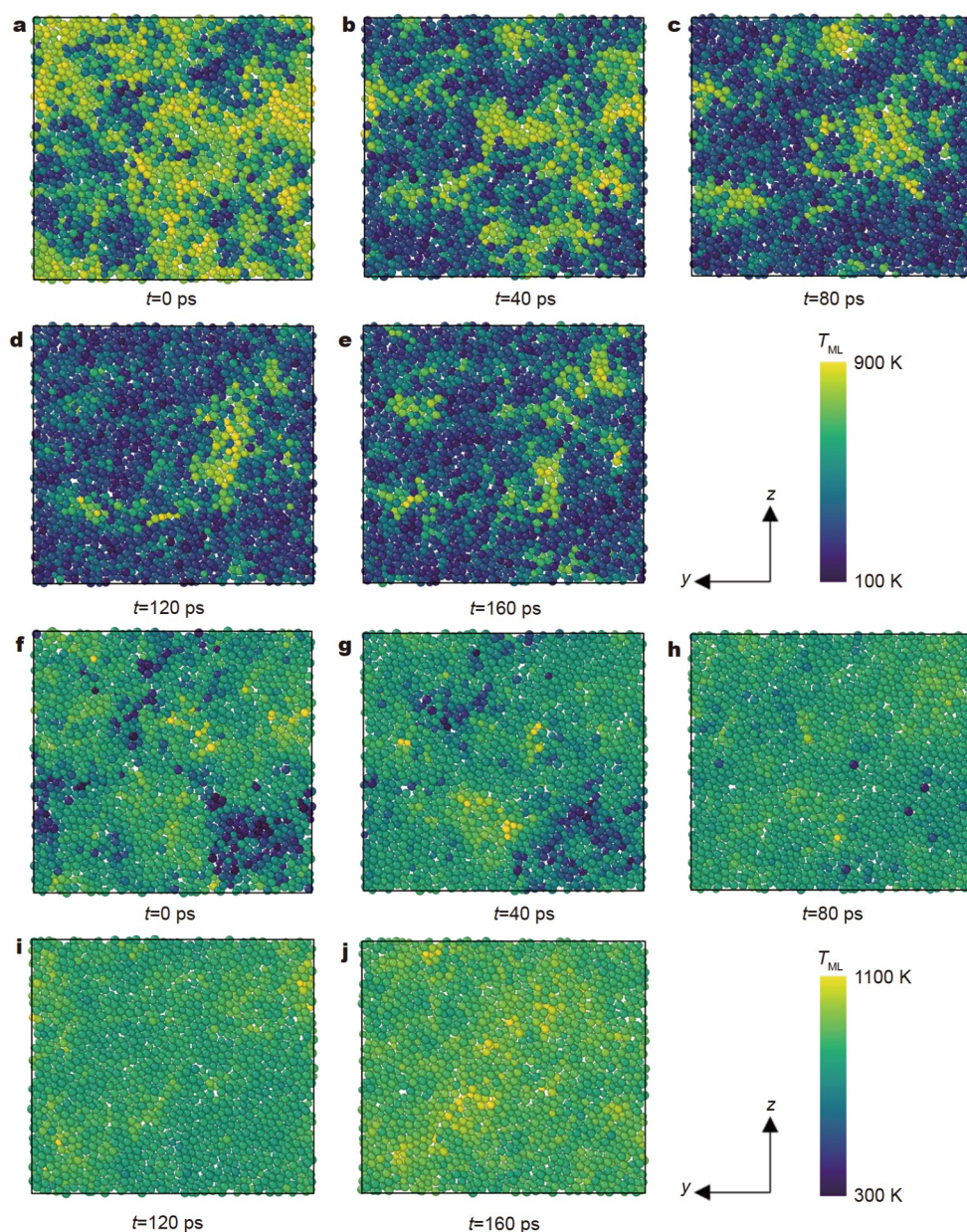


**Figure 3** Snapshots of MG slices with the thickness of 3.85 Å in a fixed position. The atoms are colored by  $T_{ML}$ . (a–e) Maps of  $T = 100$  K,  $\sigma_h = 2.2$  GPa, and  $t = 0, 40, 80, 120, 160$  ps, respectively. All the maps share the same color scale. (f–j) Results of  $\sigma_h = 2.3$  GPa.

Thirdly,  $T_{ML}$  denotes the atomic-scale spatial dynamic heterogeneity. As visualized in Fig. 3a–e, the MGs of  $\sigma_h = 2.2$  GPa always display the pronounced spatial heterogeneity in  $T_{ML}$ . The LAs actively respond to the thermal and mechanical stimuli, but they are transient. Hence the localized liquid-like regions do not settle but fluctuate frequently. On the contrary, as illustrated in Fig. 3f–j, the high-stressed MGs possess a reduced spatial heterogeneity. The sufficiently high stress activates an increased number of LAs and facilitates the connection of the localized liquid-like regions within the finite observation time. The improved atomic mobility of the system is prone to produce the stress-induced plastic flow. Similar to the stress effect, the temperature rise also attenuates dynamic heterogeneity [60], in accordance with our findings that the stress-induced dynamic heterogeneity weakens with the increase in  $T_{ML}$ .

#### Machine-learned temperature of the MGs during acoustic forming

Different from creep, acoustic forming can initiate plastic flows at low stresses and low temperatures but high frequency [24,25]. To uncover the atomistic mechanism of acousto-plastic flows of MGs, we simulated different loading frequencies and calculated  $T_{ML}$ . Under applied sinusoidal stress (with  $\sigma_0 < \sigma_y$ ), the strain oscillated accordingly. The quasistatic and low-frequency cyclic loading ( $f = 2.0 \times 10^{10}$  and  $5.0 \times 10^{10}$  Hz) showed a stable strain oscillation with constant strain amplitude  $\varepsilon_0$  (Fig. 4a). In sharp contrast, the enhanced driving frequency ( $f = 1.0 \times 10^{11}$  Hz) expedites the increase in strain amplitude. In initial cycles (e.g.,  $\sim 300$  ps), the deformation of MG sample was caused by viscoelasticity [7], in line with the strain under quasistatic loading. In the following cycles (e.g., 300–800 ps), the evident acousto-softening occurred and led to the gradual increase in  $\varepsilon_0$ , indi-



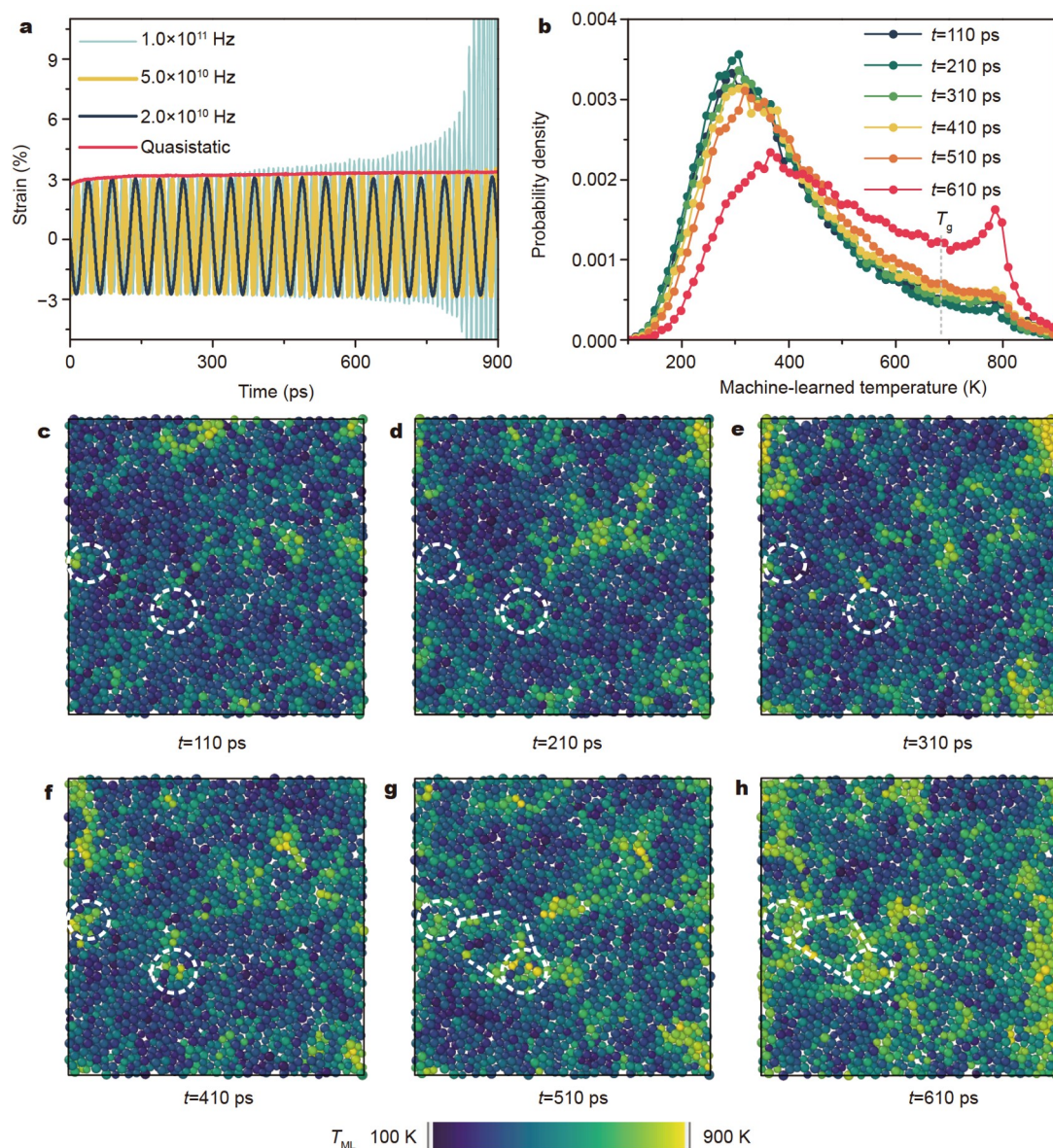


**Figure 4** Results of acoustic deformation. (a) Strain variations under cyclic and quasistatic loadings with  $\sigma_0$  or  $\sigma = 1.6$  GPa at 100 K. The driving frequencies are  $1.0 \times 10^{11}$ ,  $5.0 \times 10^{10}$ , and  $2.0 \times 10^{10}$  Hz, respectively. (b) Evolution of  $T_{ML}$  distribution during the cyclic loading. (c–h)  $T_{ML}$  maps of a slice with 3.85 Å in thickness at different time points. All the maps share the same color bar. The dashed circles and lines denote the development and interconnection of two liquid-like regions.

cating an enhanced viscous response possibly from the increased number of LAs. When  $\varepsilon_0$  approached  $\varepsilon_y$ , the deformation of MGs became unstable, and  $\varepsilon_0$  steeply climbed. Finally, the frequency-dependent acousto-plastic flow occurred. The temporal evolution of  $T_{ML}$  distribution (Fig. 4b) shows the continuous rise in high- $T_{ML}$  fraction during the acoustic deformation, signifying an increased number of LAs activated by acoustic agitations. From the  $T_{ML}$  maps in Fig. 4c–h, the isolated liquid-like regions explain the initially viscoelastic response. The continuous acoustic agitation triggers the growth and interconnection of liquid-like regions and results in acousto-plastic flow.

#### Machine-learned temperature and local plastic rearrangement

To unveil the correlation between the atomic dynamics and local plastic deformation (see Supplementary information), we com-

puted the correlation coefficients  $\rho$  between  $T_{ML}$  and non-affine squared displacement  $D_{min}^2$ , von Mises strain  $\eta^{Mises}$ , and rotation angle  $\theta$ , by  $\rho_{A,B} = \text{cov}(A,B)/(\sigma_A\sigma_B)$ , where  $A$  and  $B$  indicate the quantity,  $\text{cov}(A,B)$  is the covariance, and  $\sigma$  is the standard deviation. As shown in Fig. 5a–c, the positive  $\rho$  signals that the local plastic deformation is associated with the high- $T_{ML}$  mobile LAs, whereas the low- $T_{ML}$  immobile SAs prefer moving in an affine manner [61]. Meanwhile, the increasing  $\rho$  between  $T_{ML}$  and the local plastic rearrangement parameters over time demonstrates the closer correlation between the LAs and local plasticity. From the maps of  $T_{ML}$ ,  $D_{min}^2$ ,  $\eta^{Mises}$ , and  $\theta$  in Fig. 5d–p and Figs S4–S6, the high- $T_{ML}$  liquid-like regions gradually expand and connect. In these regions, the LAs undergo the increasingly irreversible transformations combined with the



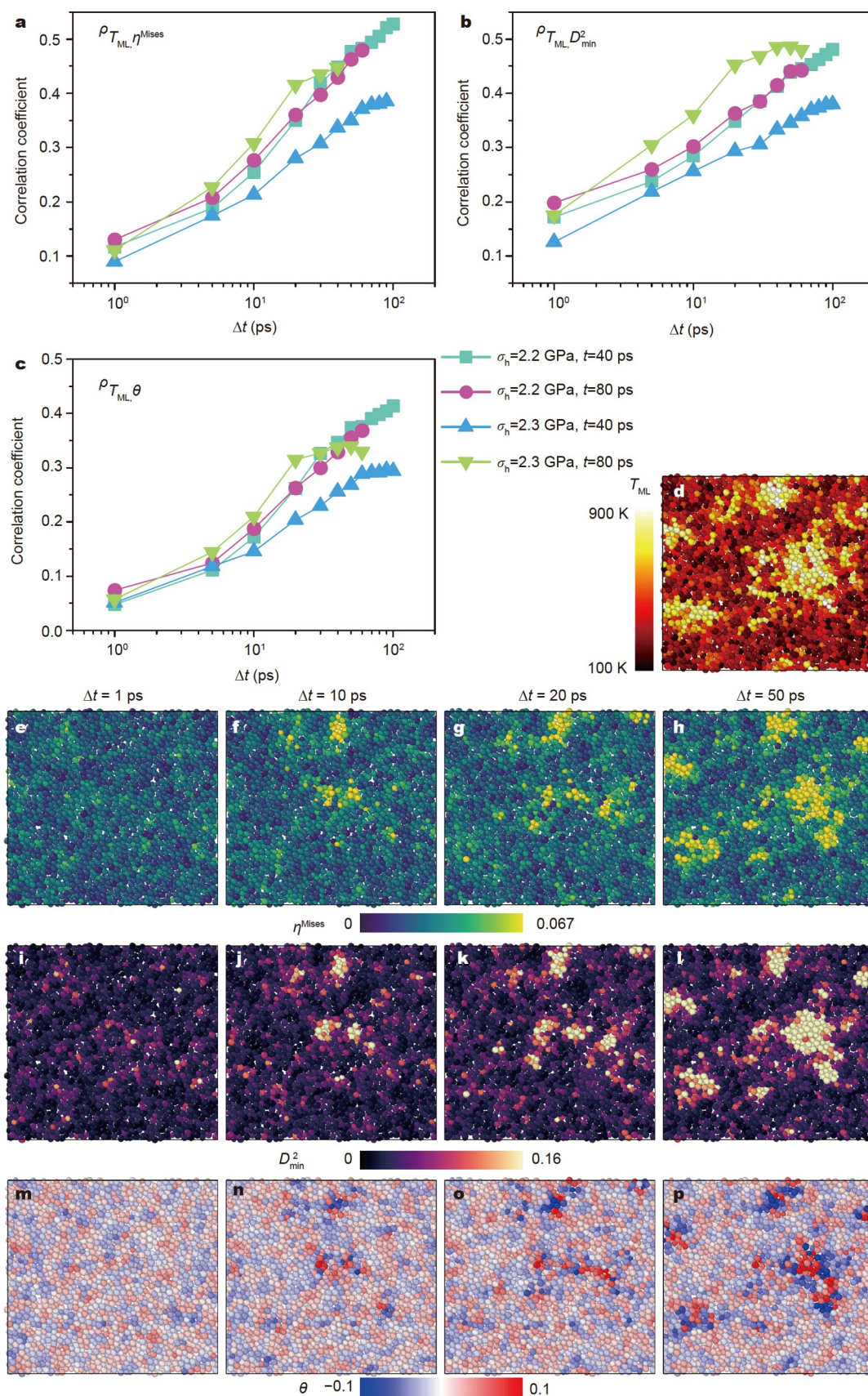


**Figure 5** Correlation coefficients between  $T_{ML}$  and (a) von Mises strain, (b) non-affine squared displacement, and (c) rotation angle. These plots display the data of various holding stresses  $\sigma_h$  and start time  $t$ . The x-axes are the time interval from the start time. (d)  $T_{ML}$  map of  $\sigma_h = 2.2$  GPa, and  $t = 80$  ps; (e–h) von Mises strain maps with different  $\Delta t$ ; (i–l) the non-affine squared displacement maps; (m–p) the rotation angle maps.

severely collective rotation of atoms [17,62]. Therefore, the atomic-scale mechanism of creep deformation is the thermally activated diffusive motion of individual atoms combined with the stress-induced collective atomic rearrangement.

### Machine-learned temperature and local structural characteristics

Because  $T_{ML}$  is obtained without relying on any structural features, it is intriguing to investigate whether  $T_{ML}$  correlates with structural features, including the Voronoi indices, the degree of local fivefold symmetry ( $d_5$ ), and the BOO parameters ( $q_6$  and  $\bar{w}_6$ ) whose definitions can be seen in Supplementary information. Here, we regarded 10% of the atoms with the highest or lowest  $T_{ML}$  as the most LAs or the most SAs, respectively. The column graphs in Fig. 6a, b statistically display the population of the top ten polyhedra types in the SAs and LAs, respectively. Interestingly, the two commonest cluster types of <0,2,8,1> and <0,2,8,2> are abundant in both SAs and LAs, which means that these two Cu-centered clusters [63] do not have the apparent bias to be solid-like or liquid-like [64]. However, arriving at a conclusion only on the grounds of population is inadequate, and it is necessary to introduce new parameters to quantify the propensity for atomic mobility. Accordingly, we proposed a parameter  $\Delta f_{LA \text{ or } SA}$  as defined by the following:

$$\Delta f_{LA \text{ or } SA} = \frac{f_{LA \text{ or } SA} - f_{total}}{f_{total}} \times 100\%, \quad (1)$$

where  $\Delta f_{LA \text{ or } SA}$  is the fraction from the LAs or SAs, and  $f_{total}$  is the fraction from the whole sample. A positive  $\Delta f_{LA \text{ or } SA}$  represents the local fraction above average and signifies the LA- or SA-favored structure, whereas a negative value denotes the opposite.

As illustrated in Fig. 6a, the Voronoi type of <0,0,12,0>, corresponding to the full icosahedron, has the highest  $\Delta f_{SA}$  of 64% and is thus the most favored local structure in the SAs. Following icosahedra, the SA-favored cluster types <0,2,8,5> and <0,1,10,4> with  $\Delta f_{SA} = 30\%$  and 29% also exhibit a highly local fivefold symmetry, with  $d_5 = 53\%$  and 67%. By contrast, the most LA-favored clusters, such as <0,4,4,3> and <0,4,4,4>, present an inferior fivefold symmetry, only having  $d_5 = 36\%$  and 33%, respectively, as shown in Fig. 6b. This finding agrees with that the structure of deformed MGs is similar to that of supercooled liquids, i.e., MGs at the temperature between  $T_g$  and liquidus [59]. According to the polytetrahedral packing model [2,61], the SA-favored clusters roughly correspond to slightly distorted Z clusters, with densely packed and geometrically stable configurations [61], whereas the LA-favored ones possibly belong to highly distorted Z clusters, i.e., the GUMs, with more loose packed “defects” or free volumes [63]. However, the clusters of <0,2,8,5> and <0,4,4,3> have the same content of disclination from Z clusters, but they are SA- and LA-favored, respectively. Another similar situation exists on the clusters of <0,1,10,4> and <0,3,6,2>. These findings indicate that similar static structures may also have the vast differences in dynamics.  $T_{ML}$  can partly correlate with local structures, and more importantly,  $T_{ML}$  contains additional dynamic information, which can illustrate the dynamic heterogeneity and origin of plasticity of MGs.

Among the BOO parameters,  $q_6$  and  $\bar{w}_6$  are very sensitive to identify the local symmetry [65,66]. As shown in Fig. 6c–e, the joint probability distributions of  $q_6$  and  $\bar{w}_6$  compare the local symmetries of SAs, LAs, and total atoms. The contour of the SAs sticks out near the icosahedron symbol, which turns out the

preference for icosahedron-like clusters, as reported in Ref. [28]. However, the contour of the LAs shrinks away from the icosahedron symbol, suggesting the local fivefold symmetry-induced inhibition of atomic mobility. The local plasticity prefers originating from the regions of less fivefold symmetric that are mostly occupied by the high- $T_{ML}$  LAs. In addition, the local crystallinity can be estimated by measuring BOO parameters  $s(i,j)$  [67] (see Supplementary information). As shown in Fig. 6f, the majority of bonds between two nearest neighbor atoms are disordered bonds, which have a lower  $s(i,j)$  than the critical value of 0.7 [67]. Compared with SAs, LAs have a tendency toward forming crystalline bonds. It is reasonable that these mobile LAs with more crystalline bonds can easily initiate the local plastic events.

### Machine-learned temperature and local chemical environment

As shown in Fig. 7a, the most LAs consist of 57% of Cu atoms and 43% of Zr atoms, but the proportion of Cu to Zr atoms is 47% to 53% for the most SAs, which agrees with Ref. [64]. Fig. 7b illustrates the degrees of deviation from complete chemical disorder ( $\alpha = 0$ ), with the favored atomic pairs indicated by negative  $\alpha$  and the unfavored pairs with positive  $\alpha$  (see Supplementary information). Clearly, the Cu-Zr pairs are more common for the Cu-centered clusters. However, a different case is observed for the Zr-centered clusters, whose Zr-Zr pairs slightly outnumber the Zr-Cu pairs. This finding is due to the preponderance of the coordination number (CN) of Zr atoms, with the average  $Z_{Zr} = 13.7$  larger than  $Z_{Cu} = 10.4$ . Measured by  $\alpha$ , the chemical short-range order shows a negligible difference between the SAs and LAs. Distinct from the reference of  $\alpha$ , the complete chemical disordered state of  $\eta$  is expressed by  $Z_{A(B)}^* = f_B Z_A Z_B / \langle Z \rangle$ , which is obtained from maximizing the entropy of mixing [68] and takes the unequal CN effect into consideration. Interestingly, the results in Fig. 7c reveal sharp contrast between the LAs and SAs. The heterogeneous Cu-Zr pairs are not only preferred in the Cu-centered clusters as described by  $\alpha$ , but also prevalent in the Zr-centered clusters for the SAs and total atoms. Note that this result is not contradictory to the findings from  $\alpha$ . The Zr-Zr pairs indeed have a greater number than the Zr-Cu pairs, but  $\eta$  eliminates the unequal CN effect and thus signals the propensity. Therefore, the heterogeneous Zr-Cu pairs are preferred, which is consistent with the negative enthalpy of mixing for Cu and Zr. The abnormal propensity of the Zr-centered clusters in the LAs is attributed to the loose-packed environment of the liquid-like regions, which leads to a drop in  $Z_{Zr}$  from 13.7 (for total atoms) to 11.7 (for LAs). In a word, the high- $T_{ML}$  LAs are mainly composed of Cu atoms, which prefer being paired with Zr atoms. The low- $T_{ML}$  SAs contain more Zr atoms, which also favor the heterogeneous Zr-Cu pairs, despite the larger number of the homogeneous Zr-Zr pairs in absolute terms.

## DISCUSSION

Given the nonequilibrium nature and slow relaxation dynamics, MGs can be viewed as the frozen liquids with extremely high viscosity. We drew on a phenomenologically mechanical model [69,70] to understand the microscale rheology of MGs, as illustrated in Fig. 8a. This model describes the combination of two viscosity mechanisms, which conceptually matches well with the dynamic heterogeneity in MGs, i.e., the LAs and SAs. Through



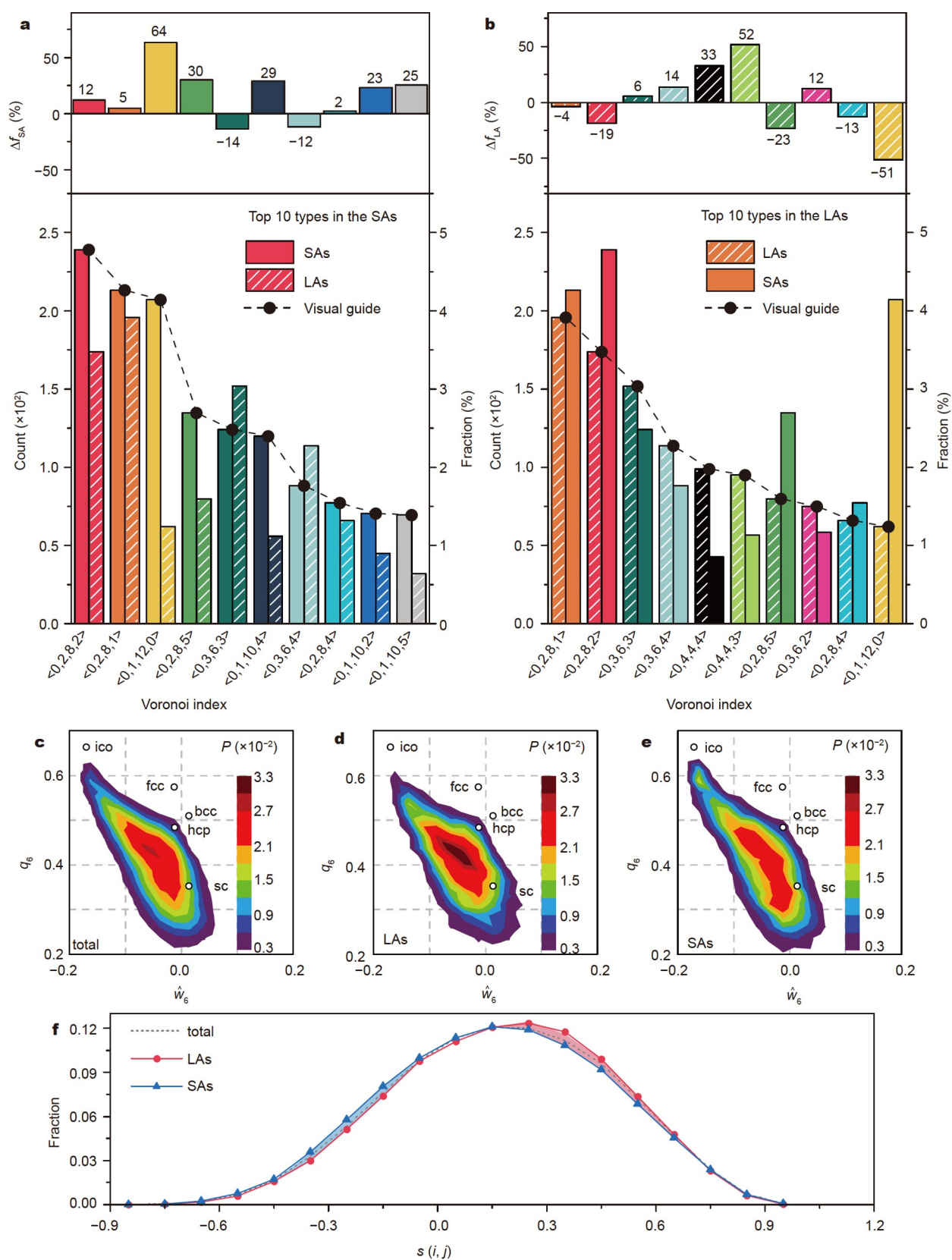


**Figure 6** Comparison of local structural characteristics of SAs and LAs. (a) Counts, fractions, and propensity parameters of the top ten Voronoi polyhedra in the SAs. Next to the SAs, the count of each cluster type in the LAs is also plotted for comparison. (b) Results for the LAs. (c) Joint probability distributions of BOO parameters in total atoms, (d) for the LAs, and (e) for the SAs. The perfect icosahedral (ico), face-centered cubic (fcc), body-centered cubic (bcc), hexagonal close packing (hcp), and simple cubic (sc) structures are labeled by open circles. (f) Probability distribution of  $s(i,j)$ . All the data presented in the figure are from the steady-state creep stage, with  $\sigma_h = 2.3$  GPa,  $T = 100$  K, and  $t = 40$  ps.



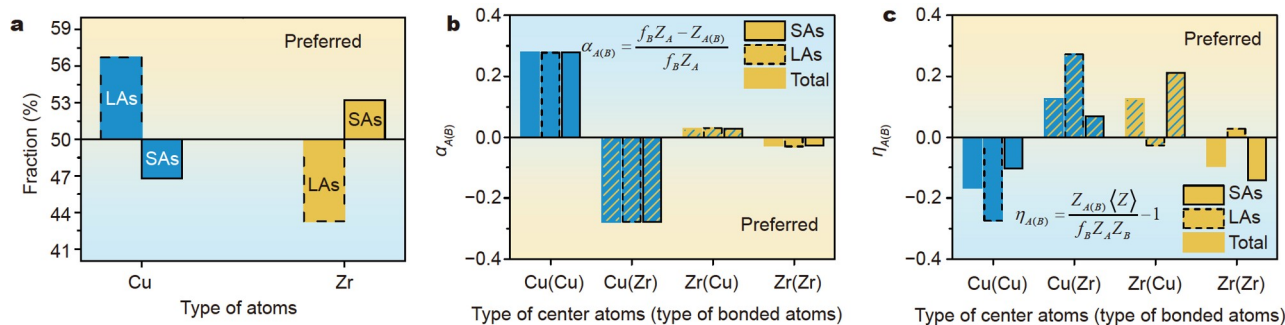


**Figure 7** Comparison of the chemical short-range order parameters in the SAs, LAs, and total atoms. (a) Atomic fractions; (b)  $\alpha_{A(B)}$ ; (c)  $\eta_{A(B)}$ . All the data presented in the figure are from the steady-state creep stage, with  $\sigma_h = 2.3$  GPa,  $T = 100$  K, and  $t = 40$  ps. The columns with the solid, dashed, and no borders represent the results for the SAs, LAs, and total atoms, respectively.

solving the Langevin equation of this model, the MSD can be derived [69,70]:

$$\langle \Delta r(t)^2 \rangle = \frac{6k_B T}{m} \frac{1}{\lambda_2 - \lambda_1} \left[ \frac{\lambda_2 + \frac{1}{\tau_2}}{\lambda_2} \left( \frac{e^{\lambda_2 t} - 1}{\lambda_2} - t \right) - \frac{\lambda_1 + \frac{1}{\tau_2}}{\lambda_1} \left( \frac{e^{\lambda_1 t} - 1}{\lambda_1} - t \right) \right] \quad (2)$$

where  $k_B$  is the Boltzmann constant,  $m$  is the average atomic mass,  $\tau_2 = m/\eta_2$ ,  $\lambda_{1,2}$  are the roots of the characteristic equation when solving the velocity autocorrelation functions,

$$\lambda_{1,2} = -(\eta_2/2m) \left( 1 + (\eta_1\eta_2/km) \pm \sqrt{(\eta_1\eta_2/km - 1)^2 - 4\eta_1^2/km} \right),$$

where  $k$ ,  $\eta_1$ , and  $\eta_2$  are the parameters from the rheological model. As shown in the log-log plot (Fig. 8b), the MSD at different temperatures can be well fitted by the model. At the small time limit ( $t \rightarrow 0$ ), Equation (2) is simplified by

$$\langle \Delta r(t)^2 \rangle \approx \frac{3k_B T}{m} t^2, \text{ corresponding to the free motion of atoms.}$$

At the large time limit ( $t \rightarrow \infty$ ), the MSD is in the diffusive mode, and Equation (2) is approximated by  $\langle \Delta r(t)^2 \rangle \approx \frac{6k_B T}{ma} t$ , where  $a$

is a constant associated with  $k$ ,  $\eta_1$ , and  $\eta_2$ . For low- $T$  glassy samples, there is a plateau of MSD in between, which is related to the caging effect. The plateau is near the level  $\langle \Delta r(t)^2 \rangle \approx \frac{6k_B T}{mb}$ , where  $b$  is a constant only tied to  $k$  [52,71,72].

From this model, the dynamic behavior of MGs can be characterized and understood by MSD, which is the reason why we applied squared displacements as the features for training the ML model. According to Equation (2), the MSD is proportional to  $T$ , and thus the curves will collapse as the data are scaled by  $T$  (see Fig. S7), which enables us to compare atomic motion behaviors regardless of the applied temperature, agreeing with our data preprocessing during ML. When the sample is under stress, such as 2.2 GPa, the caging regime becomes ephemeral, and the diffusion regime moves ahead, as shown in Fig. 8b. If the MSD is scaled by  $T$ , then it will behave like the MGs with elevated  $T$ , but it is “heated” up by the mechanical agitations. In this study, we only collected the data from one MG composition, but the model implies that our ML model is also valid to other alloy systems as long as the data are scaled by the elastic constant.

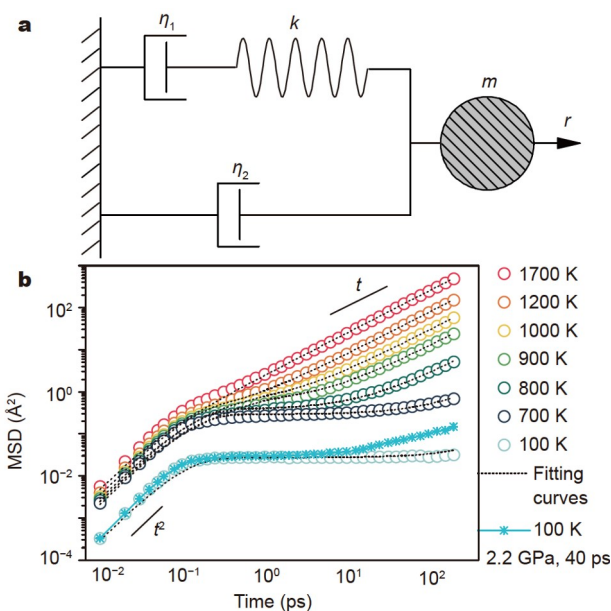


**Figure 8** Results of the rheological model. (a) Schematic of the microscale rheological model; (b) MSD evolution under different conditions.

## CONCLUSIONS

In summary, a temperature-like parameter  $T_{ML}$  has been proposed by the  $kNN$  ML model, to characterize the atomic dynamics in response to thermal, quasistatic and cyclic mechanical stimuli. Particularly, free from static local structures,  $T_{ML}$  identifies the LAs in MGs from atomic dynamics and quantitatively measures how active (“hot”) a LA is. Determined by  $T_{ML}$ , LAs bridge the fast dynamics with local plasticity, less fivefold symmetric structure, and chemical preference.  $T_{ML}$  successfully reveals the dynamic origin of plasticity of MGs, including thermoplastic and acousto-plastic flow. The microscopic rheology model illustrates the relationship between the dynamics of MGs and MSD, which suggests the validity of our parameter for other glassy systems.

Received 25 December 2021; accepted 7 February 2022;  
published online 25 March 2022

- 1 Ruta B, Pineda E, Evenson Z. Relaxation processes and physical aging in metallic glasses. *J Phys-Condens Matter*, 2017, 29: 503002

- 2 Cheng YQ, Ma E. Atomic-level structure and structure-property relationship in metallic glasses. *Prog Mater Sci*, 2011, 56: 379–473
- 3 Qiao JC, Wang Q, Pelletier JM, *et al.* Structural heterogeneities and mechanical behavior of amorphous alloys. *Prog Mater Sci*, 2019, 104: 250–329
- 4 Wang WH. The elastic properties, elastic models and elastic perspectives of metallic glasses. *Prog Mater Sci*, 2012, 57: 487–656
- 5 Suryanarayana C, Inoue A. Bulk Metallic Glasses. Boca Raton: CRC press, 2017
- 6 Yang Y, Zeng JF, Volland A, *et al.* Fractal growth of the dense-packing phase in annealed metallic glass imaged by high-resolution atomic force microscopy. *Acta Mater*, 2012, 60: 5260–5272
- 7 Ye JC, Lu J, Liu CT, *et al.* Atomistic free-volume zones and inelastic deformation of metallic glasses. *Nat Mater*, 2010, 9: 619–623
- 8 Hu YC, Li FX, Li MZ, *et al.* Five-fold symmetry as indicator of dynamic arrest in metallic glass-forming liquids. *Nat Commun*, 2015, 6: 8310
- 9 Tanaka H. Two-order-parameter model of the liquid-glass transition. III. Universal patterns of relaxations in glass-forming liquids. *J Non-Crystalline Solids*, 2005, 351: 3396–3413
- 10 Wang Z, Sun BA, Bai HY, *et al.* Evolution of hidden localized flow during glass-to-liquid transition in metallic glass. *Nat Commun*, 2014, 5: 5823
- 11 Harmon JS, Demetriou MD, Johnson WL, *et al.* Anelastic to plastic transition in metallic glass-forming liquids. *Phys Rev Lett*, 2007, 99: 135502
- 12 Debenedetti PG, Stillinger FH. Supercooled liquids and the glass transition. *Nature*, 2001, 410: 259–267
- 13 Mayr SG. Activation energy of shear transformation zones: A key for understanding rheology of glasses and liquids. *Phys Rev Lett*, 2006, 97: 195501
- 14 Guan P, Chen M, Egami T. Stress-temperature scaling for steady-state flow in metallic glasses. *Phys Rev Lett*, 2010, 104: 205701
- 15 Wang Q, Zhang ST, Yang Y, *et al.* Unusual fast secondary relaxation in metallic glass. *Nat Commun*, 2015, 6: 7876
- 16 Wang Q, Liu JJ, Ye YF, *et al.* Universal secondary relaxation and unusual brittle-to-ductile transition in metallic glasses. *Mater Today*, 2017, 20: 293–300
- 17 Liu XD, Wang TY, Ye YF, *et al.* Unusual vortex-like atomic motion observed for viscoelasticity in metallic glass. *Comput Mater Sci*, 2018, 155: 104–111
- 18 Spikes H. Stress-augmented thermal activation: Tribology feels the force. *Friction*, 2018, 6: 1–31
- 19 Johnson WL, Samwer K. A universal criterion for plastic yielding of metallic glasses with a  $(t/t_g)^{2/3}$  temperature dependence. *Phys Rev Lett*, 2005, 95: 195501
- 20 Fan Y, Iwashita T, Egami T. How thermally activated deformation starts in metallic glass. *Nat Commun*, 2014, 5: 5083
- 21 Rodney D, Schuh C. Distribution of thermally activated plastic events in a flowing glass. *Phys Rev Lett*, 2009, 102: 235503
- 22 Demetriou MD, Harmon JS, Tao M, *et al.* Cooperative shear model for the rheology of glass-forming metallic liquids. *Phys Rev Lett*, 2006, 97: 065502
- 23 Ye YF, Liu XD, Wang S, *et al.* The kinetic origin of delayed yielding in metallic glasses. *Appl Phys Lett*, 2016, 108: 251901
- 24 Ma J, Yang C, Liu X, *et al.* Fast surface dynamics enabled cold joining of metallic glasses. *Sci Adv*, 2019, 5: eaax7256
- 25 Li X, Wei D, Zhang JY, *et al.* Ultrasonic plasticity of metallic glass near room temperature. *Appl Mater Today*, 2020, 21: 100866
- 26 Spaepen F. A microscopic mechanism for steady state inhomogeneous flow in metallic glasses. *Acta Metall*, 1977, 25: 407–415
- 27 Steinhardt PJ, Nelson DR, Ronchetti M. Bond-orientational order in liquids and glasses. *Phys Rev B*, 1983, 28: 784–805
- 28 Tomida T, Egami T. Molecular-dynamics study of orientational order in liquids and glasses and its relation to the glass transition. *Phys Rev B*, 1995, 52: 3290–3308
- 29 Yang X, Liu R, Yang M, *et al.* Structures of local rearrangements in soft colloidal glasses. *Phys Rev Lett*, 2016, 116: 238003
- 30 Tong H, Tanaka H. Structural order as a genuine control parameter of dynamics in simple glass formers. *Nat Commun*, 2019, 10: 5596
- 31 Tong H, Tanaka H. Role of attractive interactions in structure ordering and dynamics of glass-forming liquids. *Phys Rev Lett*, 2020, 124: 225501
- 32 Sheng HW, Luo WK, Alamgir FM, *et al.* Atomic packing and short-to-medium-range order in metallic glasses. *Nature*, 2006, 439: 419–425
- 33 Peng HL, Li MZ, Wang WH. Structural signature of plastic deformation in metallic glasses. *Phys Rev Lett*, 2011, 106: 135503
- 34 Ma E. Tuning order in disorder. *Nat Mater*, 2015, 14: 547–552
- 35 Peng CX, Şöpu D, Song KK, *et al.* Bond length deviation in CuZr metallic glasses. *Phys Rev B*, 2017, 96: 174112
- 36 Rieser JM, Goodrich CP, Liu AJ, *et al.* Divergence of Voronoi cell anisotropy vector: A threshold-free characterization of local structure in amorphous materials. *Phys Rev Lett*, 2016, 116: 088001
- 37 Ding J, Patinet S, Falk ML, *et al.* Soft spots and their structural signature in a metallic glass. *Proc Natl Acad Sci USA*, 2014, 111: 14052–14056
- 38 Widmer-Cooper A, Perry H, Harrowell P, *et al.* Irreversible reorganization in a supercooled liquid originates from localized soft modes. *Nat Phys*, 2008, 4: 711–715
- 39 Zylberg J, Lerner E, Bar-Sinai Y, *et al.* Local thermal energy as a structural indicator in glasses. *Proc Natl Acad Sci USA*, 2017, 114: 7289–7294
- 40 Wei D, Yang J, Jiang MQ, *et al.* Revisiting the structure-property relationship of metallic glasses: Common spatial correlation revealed as a hidden rule. *Phys Rev B*, 2019, 99: 014115
- 41 Dyre JC. Colloquium: The glass transition and elastic models of glass-forming liquids. *Rev Mod Phys*, 2006, 78: 953–972
- 42 Yang J, Wang YJ, Ma E, *et al.* Structural parameter of orientational order to predict the boson vibrational anomaly in glasses. *Phys Rev Lett*, 2019, 122: 015501
- 43 Ding J, Cheng YQ, Sheng H, *et al.* Universal structural parameter to quantitatively predict metallic glass properties. *Nat Commun*, 2016, 7: 13733
- 44 Sun YT, Bai HY, Li MZ, *et al.* Machine learning approach for prediction and understanding of glass-forming ability. *J Phys Chem Lett*, 2017, 8: 3434–3439
- 45 Ward L, Agrawal A, Choudhary A, *et al.* A general-purpose machine learning framework for predicting properties of inorganic materials. *npj Comput Mater*, 2016, 2: 16028
- 46 Ren F, Ward L, Williams T, *et al.* Accelerated discovery of metallic glasses through iteration of machine learning and high-throughput experiments. *Sci Adv*, 2018, 4: eaq1566
- 47 Liu X, Li X, He Q, *et al.* Machine learning-based glass formation prediction in multicomponent alloys. *Acta Mater*, 2020, 201: 182–190
- 48 Zhou ZQ, He QF, Liu XD, *et al.* Rational design of chemically complex metallic glasses by hybrid modeling guided machine learning. *npj Comput Mater*, 2021, 7: 138
- 49 Cubuk ED, Schoenholz SS, Rieser JM, *et al.* Identifying structural flow defects in disordered solids using machine-learning methods. *Phys Rev Lett*, 2015, 114: 108001
- 50 Wang Q, Jain A. A transferable machine-learning framework linking interstice distribution and plastic heterogeneity in metallic glasses. *Nat Commun*, 2019, 10: 5537
- 51 Fan Z, Ding J, Ma E. Machine learning bridges local static structure with multiple properties in metallic glasses. *Mater Today*, 2020, 40: 48–62
- 52 Peng ZH, Yang ZY, Wang YJ. Machine learning atomic-scale stiffness in metallic glass. *Extreme Mech Lett*, 2021, 48: 101446
- 53 Yang ZY, Wei D, Zacccone A, *et al.* Machine-learning integrated glassy defect from an intricate configurational-thermodynamic-dynamic space. *Phys Rev B*, 2021, 104: 064108
- 54 Wang Q, Ding J, Zhang L, *et al.* Predicting the propensity for thermally activated  $\beta$  events in metallic glasses via interpretable machine learning. *npj Comput Mater*, 2020, 6: 194
- 55 Hirata A, Wada T, Obayashi I, *et al.* Structural changes during glass formation extracted by computational homology with machine learning. *Commun Mater*, 2020, 1: 98
- 56 Liu X, Li F, Yang Y. “Softness” as the structural origin of plasticity in disordered solids: A quantitative insight from machine learning. *Sci*



- China Mater*, 2019, 62: 154–160
- 57 Mendelev MI, Kramer MJ, Ott RT, *et al.* Development of suitable interatomic potentials for simulation of liquid and amorphous Cu-Zr alloys. *Philos Mag*, 2009, 89: 967–987
  - 58 Yu P, Bai HY, Tang MB, *et al.* Excellent glass-forming ability in simple Cu<sub>50</sub>Zr<sub>50</sub>-based alloys. *J Non-Crystalline Solids*, 2005, 351: 1328–1332
  - 59 Zemp J, Celino M, Schönfeld B, *et al.* Crystal-like rearrangements of icosahedra in simulated copper-zirconium metallic glasses and their effect on mechanical properties. *Phys Rev Lett*, 2015, 115: 165501
  - 60 Ren N, Hu L, Wang B, *et al.* Structural topological signature of high-temperature non-arrhenius crossover in metallic glass-forming liquids. *Scripta Mater*, 2021, 200: 113926
  - 61 Wang B, Luo L, Guo E, *et al.* Nanometer-scale gradient atomic packing structure surrounding soft spots in metallic glasses. *npj Comput Mater*, 2018, 4: 41
  - 62 Şopu D, Scudino S, Bian XL, *et al.* Atomic-scale origin of shear band multiplication in heterogeneous metallic glasses. *Scripta Mater*, 2020, 178: 57–61
  - 63 Wakeda M, Shibutani Y, Ogata S, *et al.* Relationship between local geometrical factors and mechanical properties for Cu-Zr amorphous alloys. *Intermetallics*, 2007, 15: 139–144
  - 64 Foroughi A, Tavakoli R, Aashuri H. Molecular dynamics study of structural formation in Cu<sub>50</sub>-Zr<sub>50</sub> bulk metallic glass. *J Non-Crystalline Solids*, 2016, 432: 334–341
  - 65 Yue X, Brechtel J, Wang F, *et al.* Deformation behavior of annealed Cu<sub>64</sub>Zr<sub>36</sub> metallic glass via molecular dynamics simulations. *Mater Des*, 2020, 191: 108660
  - 66 Hirata A, Kang LJ, Fujita T, *et al.* Geometric frustration of icosahedron in metallic glasses. *Science*, 2013, 341: 376–379
  - 67 Hu YC, Tanaka H. Physical origin of glass formation from multi-component systems. *Sci Adv*, 2020, 6: eabd2928
  - 68 Cargill Iii GS, Spaepen F. Description of chemical ordering in amorphous alloys. *J Non-Crystalline Solids*, 1981, 43: 91–97
  - 69 Raikher YL, Rusakov VV, Perzynski R. Brownian motion in a viscoelastic medium modelled by a Jeffreys fluid. *Soft Matter*, 2013, 9: 10857–10865
  - 70 Raikher YL, Rusakov VV. Theory of Brownian motion in a Jeffreys fluid. *J Exp Theor Phys*, 2010, 111: 883–889
  - 71 Mason TG, Weitz DA. Optical measurements of frequency-dependent linear viscoelastic moduli of complex fluids. *Phys Rev Lett*, 1995, 74: 1250–1253
  - 72 Li B, Lou K, Kob W, *et al.* Anatomy of cage formation in a two-dimensional glass-forming liquid. *Nature*, 2020, 587: 225–229

**Acknowledgements** This work was supported by the National Natural Science Foundation of China (52071217) and Guangdong Key Laboratory of Electromagnetic Control and Intelligent Robots.

**Author contributions** Liu X and Shen J conceived the project; Shen J supervised the project; Liu X and Lu W performed the MD simulations; Liu X and Zhou Z carried out the ML; Liu X, He Q and Tian J derived the equations; Liu X wrote the manuscript. All authors discussed the results and commented on the manuscript.

**Conflict of interest** The authors declare that they have no conflict of interest.

**Supplementary information** Details of the modelling and computation and supporting data are available in the online version of the paper.



**Xiaodi Liu** obtained his bachelor and master's degrees from Shandong University in 2012 and 2015, respectively. He received his doctoral degree from the City University of Hong Kong in 2018. He is currently a full-time associate research fellow at Shenzhen University. His research focuses on the mechanical and catalytic properties of metallic glasses.



**Jun Shen** worked at Harbin Institute of Technology from 1993 to 2011 and became a professor in 1999. During 2003 to 2005, he successively visited The University of Sydney and University of Nottingham. After working at Tongji University in 2011–2018, he joined Shenzhen University. His research focuses on the metallic glasses and light metal structural materials, including glass forming ability, mechanical behavior and mechanism, and their application to precision optical devices and electromobile motors.

## 机器学习原子运动揭示金属玻璃塑性起源: 从热塑性到超声塑性

刘晓倬<sup>1,2</sup>, 赫全锋<sup>3</sup>, 卢文飞<sup>4</sup>, 周子清<sup>3</sup>, 田锦森<sup>1</sup>, 梁丹丹<sup>5</sup>, 马将<sup>1</sup>, 杨勇<sup>3,6</sup>, 沈军<sup>1,2\*</sup>

**摘要** 金属玻璃具有无序的原子排列, 但其结构与动力学并非各处均匀。许多研究证实金属玻璃的结构与动态不均匀性对于其塑性机制至关重要。金属玻璃的“缺陷”被视为结构上疏松排布、动力学上积极响应外界刺激的区域。但迄今仍未建立明确的结构-性能关系来甄别金属玻璃中的类液缺陷。本文中, 我们基于模拟原子运动轨迹并结合机器学习提出了一种不依赖于静态结构特征的缺陷。利用k近邻机器学习模型分析并预测了不同温度下的原子运动行为, 建立了温度类标签-原子运动特征映射关系。应用这个“机器学习温度”参数理解金属玻璃在应力下的塑性流, 识别类液区原子。类液区的演化揭示了金属玻璃塑性的动态起源(包括热塑性和超声塑性), 展示了应力诱发的非均匀性和原子局域环境的关联, 为热塑性成型和超声加工提供了新见解。